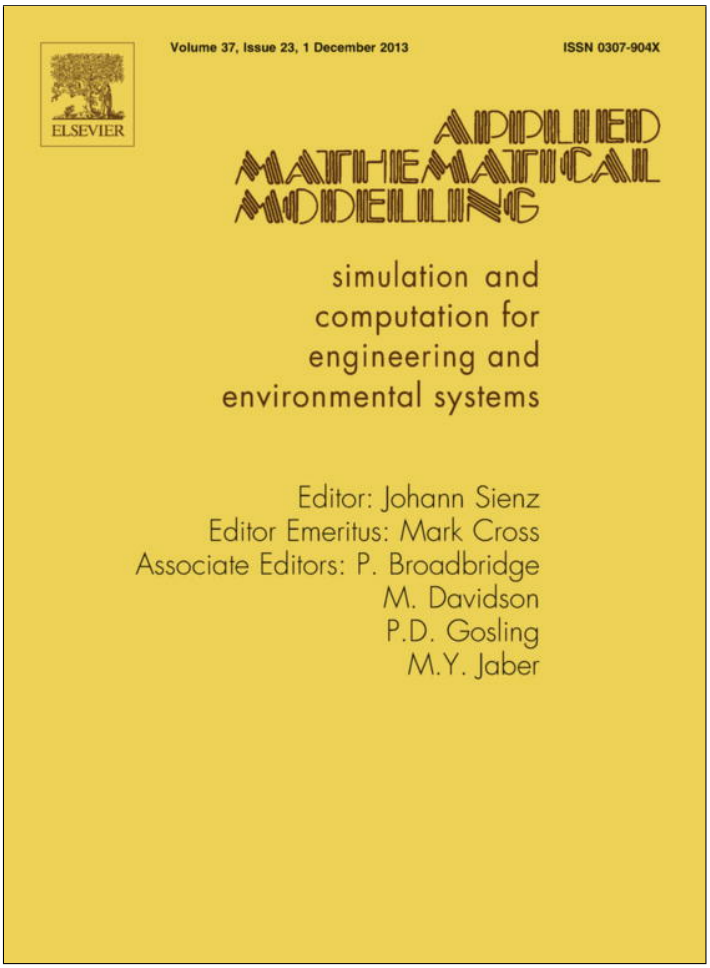

Applied Mathematical Modelling 37 (2013) 9575–9590

Contents lists available at ScienceDirect

Applied Mathematical Modelling

journal homepage: www.elsevier.com/locate/apm

Numerical study of the stability of breakwater built on a sloped porous seabed under tsunami loading

Ye Jianhong [a,c,*], Jeng Dongsheng [b,c], Wang Ren [a], Zhu Changqi [a]

[a] State Key Laboratory of Geomechanics and Geotechnical Engineering, Institute of Rock and Soil Mechanics, Chinese Academy of Sciences, Wuhan 430071, China
[b] Griffith School of Engineering, Griffith University, Gold Coast, Queensland 4222, Australia
[c] Division of Civil Engineering, University of Dundee, Dundee DD1 4HN, UK

ARTICLE INFO

Article history:
Received 25 November 2011
Received in revised form 22 April 2013
Accepted 9 May 2013
Available online 28 May 2013

Keywords:
Earthquake
Tsunami
Breakwater
Porous seabed
Shear failure
Liquefaction
Japanese 311 earthquake

ABSTRACT

Strong earthquake induced huge tsunami has occurred for three times in Pacific ocean in recent ten years; for example, the tsunami triggered by the Sumatra earthquake in 2004, Chile earthquake in 2010 and Tohoku earthquake (Japan) in 2011. Tsunami carrying huge energy always would bring high risks to the population living near to coastline. Breakwater is widely used to dissipate the wave energy, and protect coastline and ports. However, they are vulnerable when being attacked by tsunami wave. At present, the interaction mechanism between tsunami, breakwater and its seabed foundation is not fully understood. In this study, the dynamics and stability of a breakwater under the attacking of tsunami wave is investigated by adopting an integrated model PORO-WSSI 2D, in which the VARANS equation for wave motion, and the Biot's dynamic equation for soil are used. Based on the numerical results, it is found that offshore breakwater interacts intensively with tsunami wave when it overtopping and overflowing over a breakwater. The impact force on the lateral side of breakwater applied by tsunami wave is huge. The shear failure is likely to occur in the seabed foundation of breakwater. The liquefaction is unlikely to occur due to the fact that there is basically no upward seepage force in seabed foundation in the process of tsunami wave passing through the breakwater.

1. Introduction

Tsunami is frequently generated by a strong earthquake with $M_L \geqslant 6.5$ in the open sea due to the quick dislocation of a seismological fault. Tsunami carrying huge amount of energy could lead to great catastrophic losses for the properties and population in the area near to coastline where tsunami wave run-up could reach. In 2004, the tsunami triggered by the Sumatra earthquake caused numerous marine structures failed; and several hundred thousands people around the Indian ocean died. A recent case is the tsunami triggered by the Tohoku earthquake on 11 Mar 2011. More than twenty thousands people are killed; and a great number of marine facilities collapse; especially the breakwaters bulit in offshore area to protect the coastline and ports. A typical example is the Kamaishi breakwater, which was finished in 2009, and recognized as the NO. 1 in the world. This huge breakwater collapsed and failed to block the tsunami after the first attack of the huge tsunami. It resulted in the death of 935 people in Kakaishi city. Therefore, the investigation of the dynamics and stability of breakwater under the tsunami attacking is extremely important and necessary.

The investigation of wave-flat seabed interaction have been conducted widely in the past. Detailed summaries in this field can be found in Ye [1], including analytical solutions, numerical models and experimental tests. The investigation of solitary

* Corresponding author at: State Key Laboratory of Geomechanics and Geotechnical Engineering, Institute of Rock and Soil Mechanics, Chinese Academy of Sciences, Wuhan 430071, China.
E-mail address: yejianhongcas@gmail.com (J.H. Ye).

0307-904X/$ - see front matter © 2013 Elsevier Inc. All rights reserved.
http://dx.doi.org/10.1016/j.apm.2013.05.006

wave propagating on sloped coast and/or interacting with breakwater also has been conducted by researchers in the past decades. For example, Tanaka et al. [2], Li and Raichlen [3], Hsiao [4] investigated the run-up and breaking of a solitary wave on a sloped beach; however, there was no a marine structure was involved. Grilli et al. [5], Fujima [6], Huang et al. [7], Hsiao and Lin [8] investigated the interaction between the solitary wave and a breakwater built on the seabed floor. However, the dynamics of the breakwater and its seabed foundation under the solitary wave loading is completely not considered. Recently, Xiao et al. [9] develops a integrated model to investigate the breaking solitary wave-induced sediment transport on coast; additionally, the wave-induced dynamic pore pressure in the sloped seabed also can be determined by solving the Biot's consolidation equation (the acceleration of soil and pore fluid are not included). Under the same frame, the solitary wave-induced liquefaction in a sloped coast is further investigated by Young et al. [10] and Xiao et al. [11]. However, there is no a breakwater is considered; and the other dynamics of seabed floor, such as displacements, stresses, seepage flow and shear failure are completely not illustrated.

Mizutani et al. [12] and Mostafa et al. [13] developed a BEM-FEM combination numerical model to investigate the wave-seabed-structures coupling interaction. In their model, the Poisson's equations are used to govern the irrotational wave field for incompressible, inviscous fluid; and the poro-elastic Biot's consolidation equations [14,15] are used to govern the porous seabed and structures. The Poisson's equations is incapable of describing the complex motion of viscous sea water and pore water, for example, the wave breaking. Additionally, Biot's consolidation equations can only applicable for the cases in which low frequency of loading and low permeability or soil are involved. Therefore, this combined BEM-FEM model is only applicable in limited situations.

In this study, the dynamics and stability of a breakwater built on a sloped coast under tsunami wave attacking is investigated by adopting a integrated numerical model PORO-WSSI 2D [1,16], in which two sub-mdoels (wave and soil) are involved. The wave motion and the porous flow in seabed/breakwater is governed by the Volume-Averaged Reynolds Averaged Navier–Stokes (VARANS) equations; and the dynamic behaviors of the porous seabed and breakwater is governed by the dynamic Biot's equations (known as "$u-p$" approximation). The continuity of pressure and flux at the interface between seawater and the seabed/breakwater is applied to couple the two model together in numerical computation.

From the point of view of practice, the characteristics of a real tsunami wave induced by the dislocation of plate in a strong earthquake event is complicated. An important phenomenon is that there is a depressive leading edge when arriving at shoreline. Previous investigation shown that "N-wave" is suitable to approximately simulate tsunami wave. Unfortunately, the wave maker in the developed integrated numerical model PORO-WSSI 2D can not generate a "N-wave" at present. In this study, we adopt solitary wave to approximately simulate a tsunami wave interacting with breakwater. There is an important common point for solitary wave and tsunami when interacting with marine sturctures. it is that there is a great wave crest attacking marine structures. However, it must be noted that solitary wave is not identical with a real tsunami. The numerical results and conclusions may have their appropriateness only for solitary wave.

2. Integrated numerical model

2.1. Governing equation for soil

The dynamic Biot's equation known as "$u-p$" approximation proposed by Zienkiewicz et al. [17] are used to govern the dynamic response of the porous medium under wave loading, in which the relative displacements of pore fluid to soil particles are ignored, but the acceleration of the pore water and soil particles are included:

$$\frac{\partial \sigma'_x}{\partial x}+\frac{\partial \tau_{xz}}{\partial z}=-\frac{\partial p_s}{\partial x}+\rho\frac{\partial^2 u_s}{\partial t^2}, \tag{1}$$

$$\frac{\partial \tau_{xz}}{\partial x}+\frac{\partial \sigma'_z}{\partial z}+\rho g=-\frac{\partial p_s}{\partial z}+\rho\frac{\partial^2 w_s}{\partial t^2}, \tag{2}$$

$$k\nabla^2 p_s-\gamma_w n\beta\frac{\partial p_s}{\partial t}+k\rho_f\frac{\partial^2 \epsilon_v}{\partial t^2}=\gamma_w\frac{\partial \epsilon_v}{\partial t}, \tag{3}$$

where (u_s, w_s) = the soil displacements in the horizontal and vertical directions, respectively; n = soil porosity; σ'_x and σ'_z = effective normal stresses in the horizontal and vertical directions, respectively; τ_{xz}=shear stress; p_s = the pore water pressure; $\rho=\rho_f n+\rho_s(1-n)$ is the average density of porous seabed; ρ_f = the fluid density; ρ_s = solid density; k = the Darcy's permeability; g = the gravitational acceleration, γ_ω is unit weight and ϵ_v is the volumetric strain. In Eq. (3), the compressibility of pore fluid (β) and the volume strain (ϵ_v) are defined as

$$\beta=\left(\frac{1}{K_f}+\frac{1-S_r}{p_{w0}}\right), \quad \text{and} \quad \epsilon_v=\frac{\partial u_s}{\partial x}+\frac{\partial w_s}{\partial z}, \tag{4}$$

where S_r = the degree of saturation of seabed, p_{w0} = the absolute static pressure and K_f = the bulk modulus of pore water, generally, $K_f=2.24\times10^9 N/m^2$.

The finite element method is used to solve the above governing Eqs. (1)–(3). The discretized governing equations are

$$\mathbf{M}\ddot{\bar{\mathbf{u}}} + \mathbf{K}\bar{\mathbf{u}} - \mathbf{Q}\bar{\mathbf{p}} = f^{(1)}, \tag{5}$$

$$\mathbf{G}\ddot{\bar{\mathbf{u}}} + \mathbf{Q}^{\mathrm{T}}\dot{\bar{\mathbf{u}}} + \mathbf{S}\dot{\bar{\mathbf{p}}} + \mathbf{H}\bar{\mathbf{p}} = f^{(2)}. \tag{6}$$

The Generalized Newmark pth order scheme for jth order equation scheme is adopted to calculate time integration when solving the above discretized matrix equations. The definition of coefficient matrixes M, K, Q, G, S, H, $f^{(1)}$, $f^{(2)}$, and the detailed information for the numerical method to solve the Biot's equation can be found in [16,1,18].

2.2. Governing equation for wave

The flow field inside and outside of porous media is governed by the VARANS (Volume-Averaged Reynolds Averaged Navier–Stokes) equations [19], which are derived by integrating the RANS equations over a control volume. The mass and momentum conservation equations can be expressed as:

$$\frac{\partial\langle\overline{u}_{fi}\rangle}{\partial x_i} = 0, \tag{7}$$

$$\frac{\partial\langle\overline{u}_{fi}\rangle}{\partial t} + \frac{\langle\overline{u}_{fj}\rangle}{n(1+c_A)}\frac{\partial\langle\overline{u}_{fi}\rangle}{\partial x_j} = \frac{1}{1+c_A}\left[-\frac{n}{\rho_f}\frac{\partial\langle\overline{p}\rangle^f}{\partial x_i} - \frac{\partial\langle\overline{u'_{fi}u'_{fj}}\rangle}{\partial x_j} + \frac{1}{\rho_f}\frac{\partial\langle\overline{\tau}_{ij}\rangle}{\partial x_j} + ng_i\right] - \frac{\langle\overline{u}_i\rangle}{1+c_A}\left[\frac{\alpha(1-n)^2}{n^2 d_{50}^2} + \frac{\beta(1-n)}{n^2 d_{50}}\sqrt{\langle\overline{u}_{f1}\rangle^2 + \langle\overline{u}_{f2}\rangle^2}\right], \tag{8}$$

where u_{fi} is the flow velocity, x_i is the Cartesian coordinate, t is the time, ρ_f is the water density, p is the pressure, τ_{ij} is the viscous stress tensor of mean flow, g_i is the acceleration due to gravity, and n and d_{50} are the porosity and the equivalent mean diameter of the porous material. c_A denotes the added mass coefficient, calculated by $c_A = 0.34(1-n)/n$. $\alpha = 200$ and $\beta = 1.1$ are empirical coefficients associated with the linear and nonlinear drag force, respectively [20]. More detail information on the determination of the empirical coefficients α and β can be found in [21].

"$\langle\rangle$" and "$\langle\rangle^f$" stand for Darcy's volume averaging operator and the intrinsic averaging operator, respectively, which are defined as

$$\langle a\rangle = \frac{1}{V}\int_{V_f} a\,\mathrm{d}v, \quad \text{and} \quad \langle a\rangle^f = \frac{1}{V_f}\int_{V_f} a\,\mathrm{d}v, \tag{9}$$

where V is the total averaging volume, and V_f is the portion of V that is occupied by the fluid. The relationship between the Darcy's volume averaging operator and intrinsic volume averaging is $\langle a\rangle = n\langle a\rangle^f$.

In the VARANS equations, the interfacial forces between the fluid and solids have been modeled according to the extended Forchheimer relationship, in which both linear and nonlinear drag forces between the pore water and the skeleton of porous structures are included in the last term of Eq. (8). More detailed informations of the RANS and VARANS models are available in [22,19].

The influence of turbulence fluctuations on the mean flow, denoted as $\langle u'_{fi}u'_{fj}\rangle$, is obtained by solving the volume-averaged $k-\epsilon$ turbulence model. The volume-averaged $k-\epsilon$ equations for the volume-averaged turbulent kinetic energy k and its dissipation rate ϵ of the porous flow in porous structures which are derived by taking the volume-average of the standard $k-\epsilon$ equations are expressed as

$$\frac{\partial\langle k\rangle}{\partial t} + \frac{\langle\overline{u}_{fj}\rangle}{n}\frac{\partial\langle k\rangle}{\partial x_j} = \frac{\partial}{\partial x_j}\left[\left(\frac{\langle\nu_t\rangle}{\sigma_k} + \nu_k\right)\frac{\partial\langle k\rangle}{\partial x_j}\right] - \frac{\langle\overline{u'_{fi}u'_{fj}}\rangle}{n}\frac{\partial\langle\overline{u}_{fi}\rangle}{\partial x_j} - \langle\epsilon\rangle + n\epsilon_\infty, \tag{10}$$

$$\frac{\partial\langle\epsilon\rangle}{\partial t} + \frac{\langle\overline{u}_{fj}\rangle}{n}\frac{\partial\epsilon}{\partial x_j} = \frac{\partial}{\partial x_j}\left[\left(\frac{\langle\nu_t\rangle}{\sigma_\epsilon} + \nu_k\right)\frac{\partial\epsilon}{\partial x_j}\right] - C_{1\epsilon}\frac{\langle\epsilon\rangle}{n\langle k\rangle}\langle\overline{u'_{fi}u'_{fj}}\rangle\frac{\partial\langle\overline{u}_{fi}\rangle}{\partial x_j} - C_{2\epsilon}\frac{\langle\epsilon\rangle^2}{\langle k\rangle} + nC_{2\epsilon}\frac{\epsilon_\infty^2}{k_\infty}, \tag{11}$$

the definition and determination of other parameters in Eqs. (10) and (11) could be referred to [19]

The above VARANS equations for flow field outside and inside of porous seabed are solved by using the finite difference two-step projection method on a staggered grid system for the space discretization, and the forward time difference method for the time derivative. The VOF method is applied to track water free-surface. The combined central different method and upwind method are used to solve the $k-\epsilon$ equations. In the numerical wave tank, the method of mass source function is adopted to generate the expected wave train at the position of wave maker. For solitary wave, the expression of source function can be found in [23].

2.3. Integration method

In this integrated numerical model, the wave model is adopted to generate the ocean wave, and to govern the propagating of wave on porous seabed and the seepage flow in porous seabed/structures. The flow fields outside and inside the porous seabed/structures are coupled through the continuity of pressure and velocity of water particles on the surface of seabed in wave model. Therefore, the flow field in the whole computational domain is fully coupled. In this study, a coupling algorithm is used to integrate the wave model and the soil model. In the *n*th time step, the wave model first determines the flow fields outside and inside the porous seabed, and the wave pressure acting on seabed. Secondly, the soil model obtains the pressure acting on seabed/structures determined by wave model, and then calculates the seabed responses, including effective stresses, displacements and pore pressure by taking the pressure acting on seabed as the stress boundary conditions. The detail coupling process is demonstrated in Fig. 1. The more detailed information about this integrated numerical model PORO-WSSI 2D can be found in Ye [1].

2.4. Verification of integrated model

The validity and reliability of the developed integrated numerical model PORO-WSSI 2D have been widely verified by Ye [1]. By adopting the analytical solution proposed by Hsu and Jeng [24], and a series of laboratory wave flume tests conducted by Lu [25] for regular wave and cnoidal wave, Tsai and Lee [26] for standing wave, Mizutani et al. [12] for submerged breakwater, and Mostafa et al. [13] for composite breakwater, the developed integrated numerical model PORO-WSSI 2D was used to predict the dynamic response of seabed foundation and/or breakwater. The good agreement between the numerical predicted results and the experimental data indicates that PORO-WSSI 2D is highly reliable for the problem of Wave-Seabed-Structure Interaction. More detailed information about the verification work can be found in Ye [1]; and related works have been published in Jeng et al. [27].

3. Boundary conditions

The computational domain and dimension sizes are shown in Fig. 2. A rubble mound breakwater is constructed on a sloped seabed (gradient angle 2:100). An impermeable concrete block is placed on the top of the rubble mound breakwater. The total length of the computational domain is 900 m. The distance from the breakwater to the left and right lateral side of the seabed is 500 m and 370 m, respectively. These two distance is enough to eliminate the effect of the lateral boundary condition on the stress fields in the zone near to the breakwater. In this study, following boundary conditions are applied in computation.

(1) The bottom of seabed foundation is treated as rigid and impermeable:

$$u_s = w_s = 0 \quad \text{and} \quad \frac{\partial p_s}{\partial z} = 0 \quad \text{at} \quad z = 0 \tag{12}$$

(2) The two lateral sides of seabed are fixed in x direction:

$$u_s = 0 \quad \text{at} \quad x = -300\ \text{m} \quad \text{and} \quad x = 600\ \text{m} \tag{13}$$

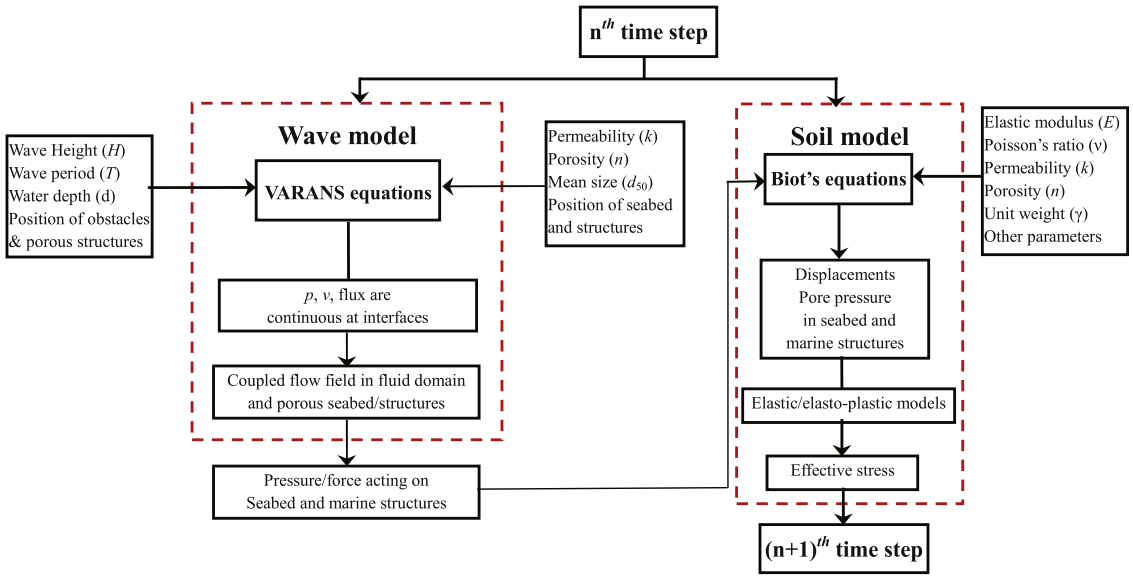

Fig. 1. The coupling precess adopted in the integrated model PORO-WSSI II.

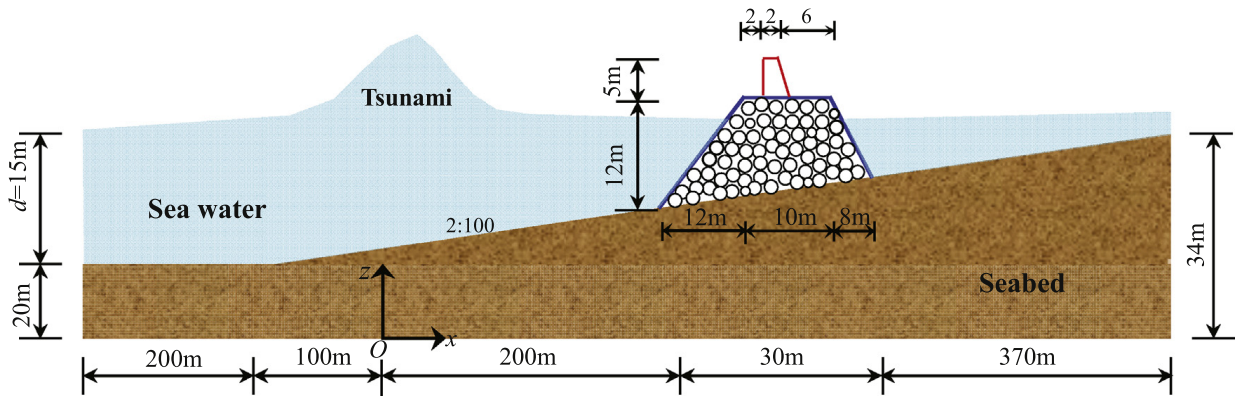

Fig. 2. The sketch map of the computational domain adopted in this study.

(3) The surface of seabed, and the outer surface of the rubble mound breakwater, concrete block are applied perpendicularly by the hydrostatic pressure, as well as the wave-induced dynamic pressure. The pore pressure is continuous at the interfaces between the seabed, breakwater and the sea water.
(4) When the tsunami wave arriving at the breakwater, there is a upward floating force acting on the bottom of the concrete block. This floating force is considered in this study. If the free surface of sea water is lower than the bottom of concrete block, for example, at the initial state, the floating force is 0.

4. Results and analysis

In this section, the dynamic response of the breakwater and its seabed foundation under tsunami wave loading is investigated. The computational domain is shown in Fig. 2. The property parameters of the seabed foundation, breakwater and concrete block used in computation are listed in Table 1. Totally 25142 8-nodes iso-parametric elements are used to discretize the domains of seabed foundation, breakwater and concrete block. Among them, the slip elements are used in the interface zones between the seabed foundation and the breakwater, and between the breakwater and the concrete block, to simulate the contact effect. The water depth, and the wave height of tsunami is 15 m and 8 m, respectively over the flat seabed. The grid size in fluid domain is maximumly 0.5 m in the region far away from the breakwater, and minimunly 0.35 m in the region closed to the breakwater in the x direction. At the mean time, The grid size in solid domain is maximumly 2.0 m in the region far away from the breakwater, and minimunly 0.5 m in the region closed to the breakwater in the x direction. The gird size in the y direction is about 1/3–1/2 of the size used in the x direction. According to the comprehensive convergence analysis for the developed numerical model PORO-WSSI 2D in [16], it is indicated that the grid size must be less than $L/200$ in fluid domain, and less than $L/40$ in solid domain, where L is a characteristic length, generally L is the wave length. Based on the formulation determining the effective wave length of solitary wave proposed by Nakayama [28]: $L = 9.5776d\sqrt{d/H}$, the effective wave length of solitary wave involved in this study is $L = 196.7$ m. The maximum grid size in fluid domain (=0.5 m) and in solid domain (=2.0 m) is significantly less than $L/200$ and $L/40$, respectively. The numerical results in fluid and solid domain are both expected to be convergent. The internal wave maker is located at x=-500 m, where is far away from the breakwater about 700 m. This long distance could make the generated solitary wave become more mature and stable before arriving at the breakwater. The FEM mesh system used to discretize the breakwater and seabed foundation is shown in Fig. 3.

4.1. Consolidation of seabed foundation

In the offshore environment, the seabed generally has experienced the consolidation process under the seawater loading and the self-gravity in the geological history. Additionally, after the breakwater is constructed on the seabed, the seabed beneath and near to the composite breakwater will be compressed, and deform under the gravity of breakwater. Finally, a new balanced state will be reached. From the point of view of physics, in order to simulate the interaction between the tsunami, seabed and breakwater, the initial consolidation state of the seabed foundation under hydrostatic pressure and the gravity of

Table 1
Properties of seabed foundation, breakwater and concrete block used in computation

Medium	E (N/m^2)	v	k (m/s)	n	Sr
Seabed foundation	3.0×10^7	0.3333	1.0×10^{-5}	0.3	0.98
Rubble mound breakwater	1.0×10^9	0.3333	2.0×10^{-1}	0.35	0.99
Concrete block	1.0×11^{10}	0.25	0.0	0.0	0.0

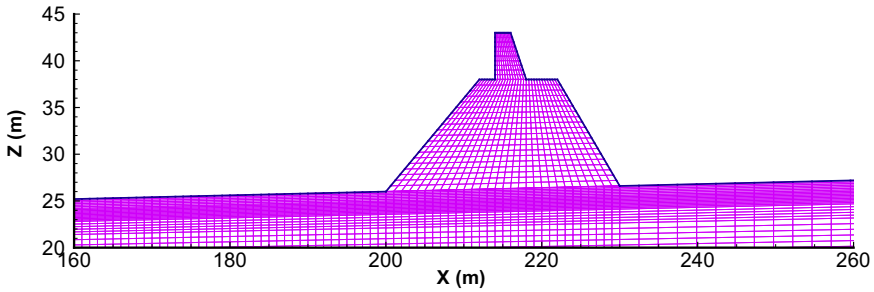

Fig. 3. FEM mesh system used in the domain of the breakwater and its seabed foundation in computation. Noted: only the range of x = 160 m–260 m is shown. The full range of the seabed is x = −300 m–600 m.

breakwater should be firstly determined. Then, this consolidation status is taken as the initial condition for the followed dynamic analysis.

Fig. 4 shows the final consolidation status of the seabed foundation under the loading of hydrostatic water pressure and the weight of breakwater (It is noted that only the results in the range x = 160 m to 260 m are shown). From Fig. 4, it is found that the pore pressure in the seabed foundation and breakwater is layered; and the pore pressure in the breakwater

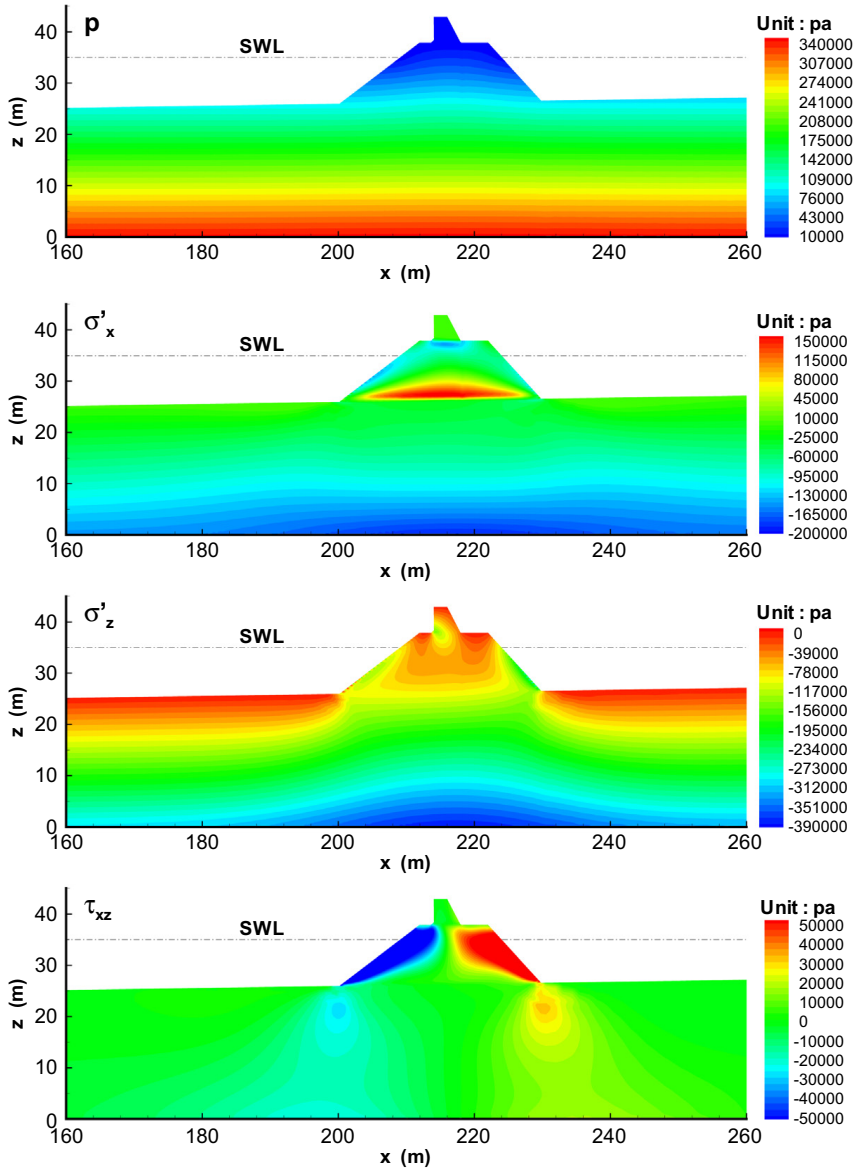

Fig. 4. Distribution of effective stresses σ'_x, σ'_z and τ_{xz}, and pore pressure p in seabed foundation and breakwater in consolidation status.

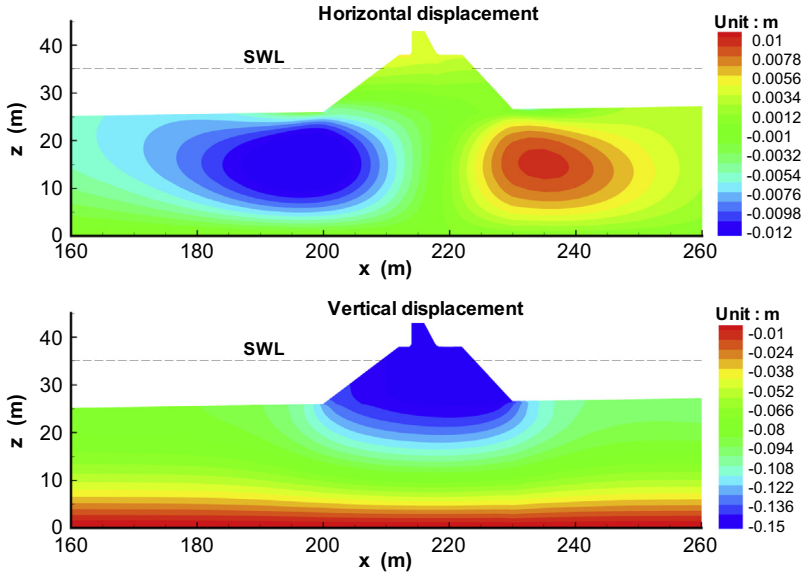

Fig. 5. Distribution of displacement in seabed foundation and breakwater in consolidation status.

over the static water level is zero. The effective stress σ'_x and σ'_z increase significantly in the zone under the rubble mound breakwater. In the region far away the breakwater, the effect of breakwater on the effective stresses gradually disappear. The distribution is also layered in the zones far away from the breakwater. In the bottom of the rubble mound breakwater, there is a zone in which the σ'_x is tensile. This phenomenon could attribute to that the stiffness of the seabed foundation and the breakwater is significantly different. The extension of the seabed foundation toward its two lateral sides will drag the bottom of the breakwater also moving toward left and right sides. The distribution of shear stress τ_{xz} illustrates that the there are two shear stress concentration zones in the seabed foundation under the breakwater. In the breakwater, the shear stress in the zone near to the two sloped sides is also huge. This is a potential harmful factor for the breakwater part collapsing.

Fig. 5 is the distribution of displacements in the seabed foundation and breakwater in the consolidation status. It is found that the seabed foundation moves toward its left and right sides, and subsides downward under the breakwater and hydrostatic pressure loading. Due to the fact that the breakwater is built on a sloped seabed, the magnitude of displacement toward left side is greater than that toward right side. The final settlement of breakwater is about 155 mm. In the region far away from the breakwater, the seabed subsides about 85 mm only under the hydrostatic pressure loading.

4.2. Interaction between tsunami wave and breakwater

The wave model in PORO-WSSI 2D is used to generate the tsunami wave, and to simulate the propagation, reflection and overtopping in the sea water. Fig. 6 demonstrates the interaction process between the tsunami wave, porous seabed and the rubble mound breakwater. The wave maker generates the tsunami wave with the height of 8 m in the seawater with the depth of 15 m at a place far away from the breakwater. After being generated, the tsunami wave propagates toward the breakwater with a very fast velocity. At time $t = 40$ s, the tsunami propagates to the place near to the breakwater. At time $t = 44$ s, the tsunami arrives at the breakwater, and begins to collide with the breakwater. Due to the blocking effect of the breakwater, the tsunami wave is breaking, overtopping at time $t = 47$ s. A huge impact force is applied on the left side of the breakwater and the concrete block by the breaking tsunami wave. The free surface of sea water in the rubble mound breakwater becomes a curve from a line. One second later ($t = 48$ s), the splashed sea water falls down; and the sea water overflows from the left-hand side of the breakwater to its right-hand side. The original static sea water at the right-hand side of the breakwater is disturbed by the sea water falling down from air, and overflowing from the left-hand side of the breakwater. The free surface of the sea water in this zone vibrates freely and irregularly. The free surface of the sea water in the breakwater looks like a closed curve; some air is trapped in this zone. At time $t = 52$ s, part of the wave energy carried by the tsunami wave is reflected by the breakwater; and the irregular vibration of the free surface of the sea water at the right-hand side of the breakwater propagates toward the coastal line. At this time, the free surface of the sea water in the breakwater basically overlaps with the top boundary of top breakwater. It means that the breakwater is full of sea water at time $t = 52$ s. In the long time after $t = 52$ s, the free surface of the sea water at left-hand side of the breakwater also vibrates freely; the amplitude of vibration decrease gradually. The free surface of the sea water in the breakwater also gradually returns to its static status. The free surface of the sea water at the right-hand sides of breakwater continuously vibrates; and this vibration propagates to the coastal line. However, the magnitude of vibration near to the breakwater also decrease gradually.

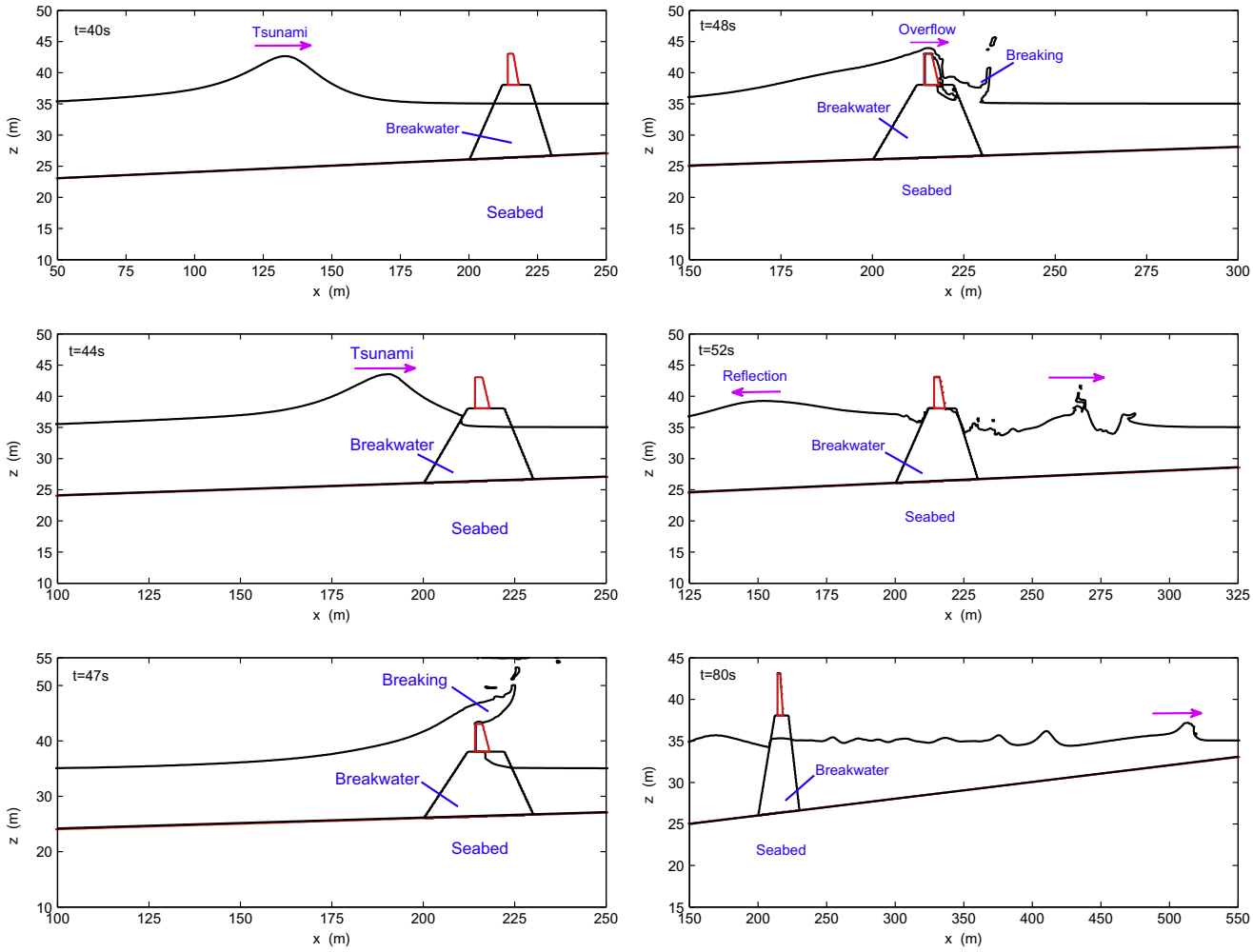

Fig. 6. Interaction process between the tsunami wave and the breakwater built on the porous seabed.

4.3. Dynamic response of breakwater

From the above analysis of the interaction process between the tsunami wave, the breakwater and concrete block, we know that there is a intensive interaction when the tsunami wave collides with the breakwater. The tsunami wave breaks, and is reflected in front of the breakwater; and overtop the breakwater. The dynamic response of the breakwater under wave loading, especially the tsunami wave loading, is one of the main problems concerned by coastal engineers involved in design work. In this section, the dynamic response of the breakwater and concrete block under the tsunami wave loading is demonstrated.

Fig. 7 illustrates the time history curves of the displacements of the concrete block and the rubble mound breakwater at their top-right corner. As illustrated in Fig. 7, it is observed that the breakwater keeps static state before the tsunami wave arriving. Once the tsunami wave arriving at time $t = 44$ s, the breakwater moves about 80 mm toward right side, and about 25 mm downward in a short period under the loading of tsunami wave. It is indicated that the tsunami wave-induced impact force on the lateral sides of the rubble mound breakwater and concrete block is huge. The impact force acting on the left lateral side of the rubble mound breakwater have two components. One pushes the breakwater toward right side; another compresses the breakwater downward. That is why the breakwater and concrete block move toward right side and downward. As the time passing, the tsunami wave breaks in front of and over the breakwater. Part of the wave energy is reflected; and the breaking tsunami wave overtops the breakwater. The reflected wave and the overtopping sea water make the free surfaces of the sea water near to the two lateral sides of the breakwater vibrate freely. The magnitude of the vibration of the free surface decreases gradually due to the energy dissipation. The free vibration of the free surface of the sea water near to the breakwater leads to that the breakwater and the concrete block also vibrates correspondingly; and the magnitude of the vibration also gradually decreases. The tsunami wave- induced horizontal displacement of the concrete block reaches up to 110 mm. It is indicated that the impact force on lateral sides of concrete block is greater than that on breakwater.

Fig. 8 demonstrates the time history curves of the pore pressure at typical point A, B, C, D and E on/in the breakwater and concrete block under the tsunami wave loading. Among these points, A, D and F are over the static water level. Before

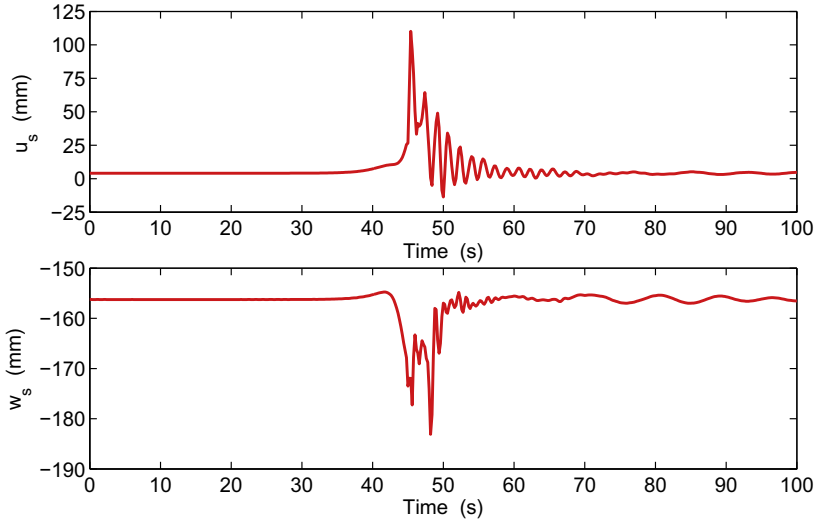

(a) Top-left corner of concrete block

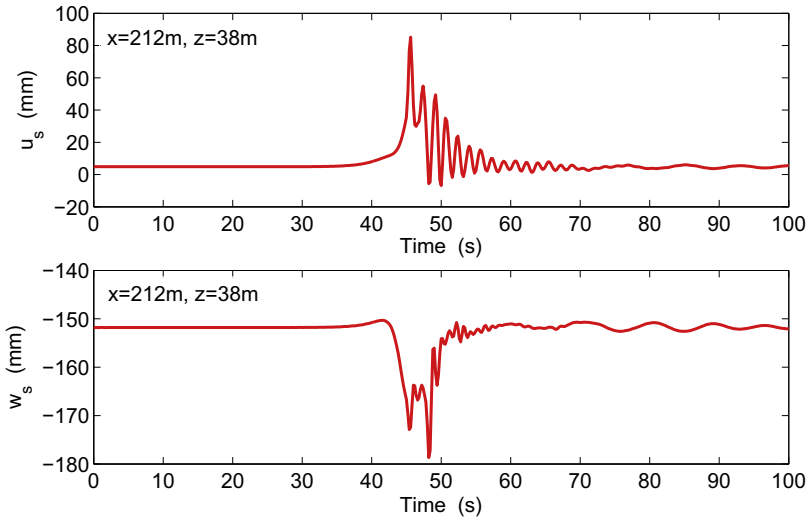

(b) Top-left corner of rubble mound breakwater

Fig. 7. Horizontal and vertical displacement of typical point on the concrete block and breakwater.

the tsunami wave arriving at the breakwater (0–44 s), and after the tsunami wave disappearing (50–100 s), there is no water pressure acting on the three points. From Fig. 8, it can be observed that the tsunami wave applies huge impact force on the left lateral sides of the breakwater and concrete block during the process of breaking, reflecting and overtopping. The maximum impact force reaches up to 136 kPa, 87 kPa and 84 kPa, respectively at point F, A and B. The impact force acting on the concrete block is much greater than that on the rubble mound breakwater. The dynamic pressure acting on the point C and D attributes to the overtopping and overflow of the sea water from the left-hand side of the breakwater to its right-hand side. The maximum impact force on C and D reach up to 105 kPa and 65 kPa, respectively. The point E is located in the breakwater. It is found that the pore pressure at point E is significantly affected by the tsunami wave when breaking, overtopping the breakwater. The point B, C and E is under the static water level. The pressure on them vibrates after time $t = 50$ s due to that the free surface of the sea water vibrates freely at the right/left hand side of the breakwater.

4.4. Dynamic response of seabed foundation

It has been documented that the wave-induced liquefaction and shear failure in seabed foundation are the mains reason for the instability of marine structures built on porous seabed. Besides the dynamic response of the breakwater, the dynamic response of the seabed foundation under the tsunami wave loading is also an important issue in the practice of engineering. In this section, the dynamic response of the seabed foundation under the tsunami wave loading is demonstrated. Here, the dynamic response at two typical times $t = 44$ s and $t = 48$ s are chosen to illustrate the tsunami wave-induced effective

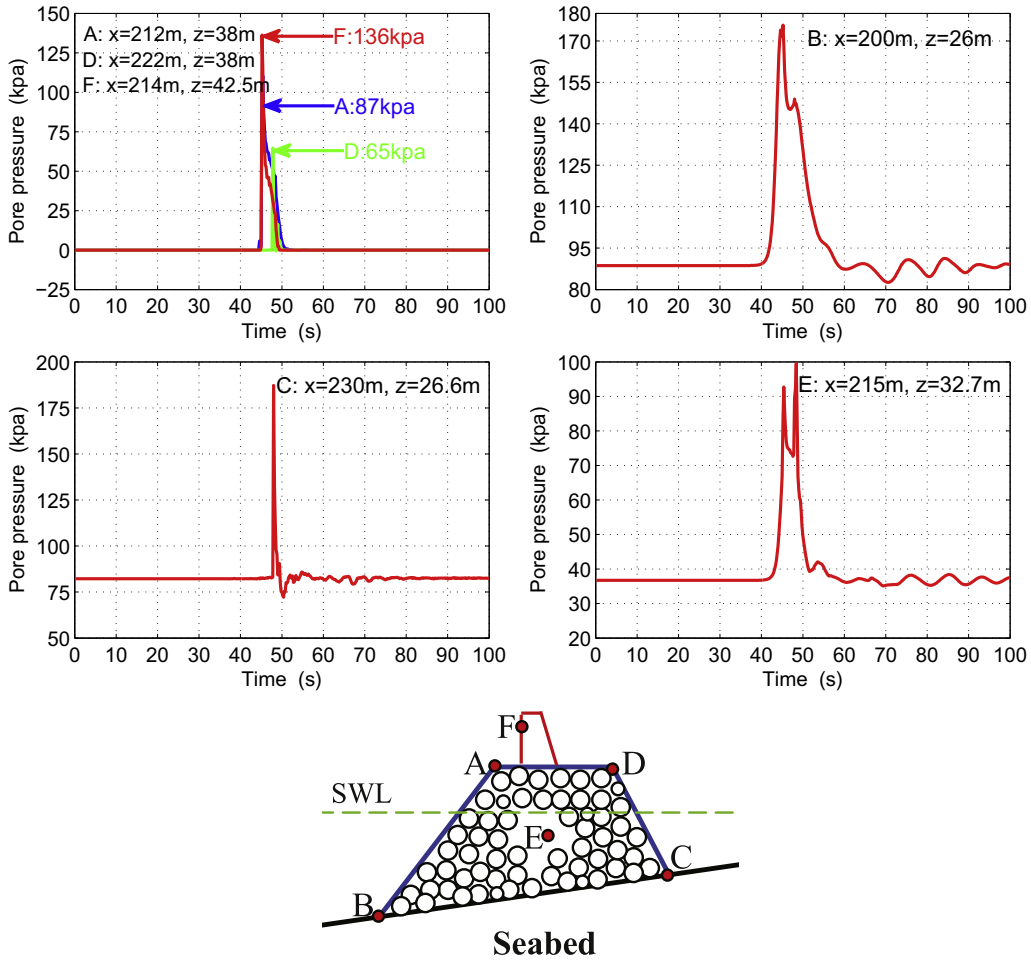

Fig. 8. Pore pressure at typical point A, B, C, D and E on/in the breakwater and concrete block.

stresses and pore pressure. At $t = 44$ s, the tsunami wave arrives at the rubble mound breakwater; and begins to collide with the breakwater. At $t = 48$ s, the tsunami wave is breaking, and overtopping the breakwater.

Figs. 9 and 10 show the tsunami wave-induced effective stresses and pore pressure in the seabed foundation and the rubble mound breakwater at times $t = 44$ s and $t = 48$ s. From Figs. 9 and 10, it is observed that the tsunami wave-induced dynamic pore pressure is significant in the zone under the crest of tsunami wave. In the region far away from the crest of tsunami wave, there is basically no the dynamic pore pressure. Due to that the rubble mound breakwater is treated as porous medium with huge permeability in computation, the dynamic pore pressure in the breakwater is also significant. Under the crest of tsunami wave, the dynamic σ'_z and σ'_y are compressive. At $t = 48$ s, there is no visible crest. The dynamic σ'_z and σ'_y in the zone under the lower right foot of the breakwater are obviously greater than that in the other zone. Due to the fact that the tsunami wave always applies a push force on the lateral sides of the breakwater and the concrete block, the breakwater has the potential to move toward right side in the process of interaction. It results in that the dynamic σ'_x in the zone of the seabed foundation near to the left-hand side of the breakwater is tensile; while, the dynamic σ'_x is compressive in the zone near to the right-hand side of breakwater. It also leads to that there is also a zone in which the compressive dynamic σ'_x and σ'_y are generated in the bottom of the breakwater. The variation process of shear stress in the zone near or under the rubble mound breakwater is the most important issue due to that the shear failure of seabed foundation is directly related to it. It is found that the tsunami wave not only affects the shear stress in the breakwater, but also in the seabed foundation. At $t = 44$ s, the dynamic shear stress mainly concentrates in the zone under the left-half part of the breakwater. As the tsunami wave breaking, overtopping the breakwater, the shear stress concentration zone also moves toward right. At $t = 48$ s, the dynamic shear stress concentrates in the zone under the right-half part of breakwater. From the above analysis, it is found that the effect of tsunami wave on the pore pressure and effective stresses in the seabed foundation is very significant. The dynamic response of the seabed foundation, including the tsunami wave-induced dynamic pore pressure and effective stresses, variates corresponding to the position and state of the tsunami wave in the process of interaction between the tsunami wave, breakwater and seabed foundation.

Figs. 9 and 10 only show the dynamic response of the seabed foundation and breakwater under the tsunami wave loading at the two typical times $t = 44$ s and $t = 48$ s. Fig. 11 illustrates the time history curve of the dynamic pore pressure p_s and

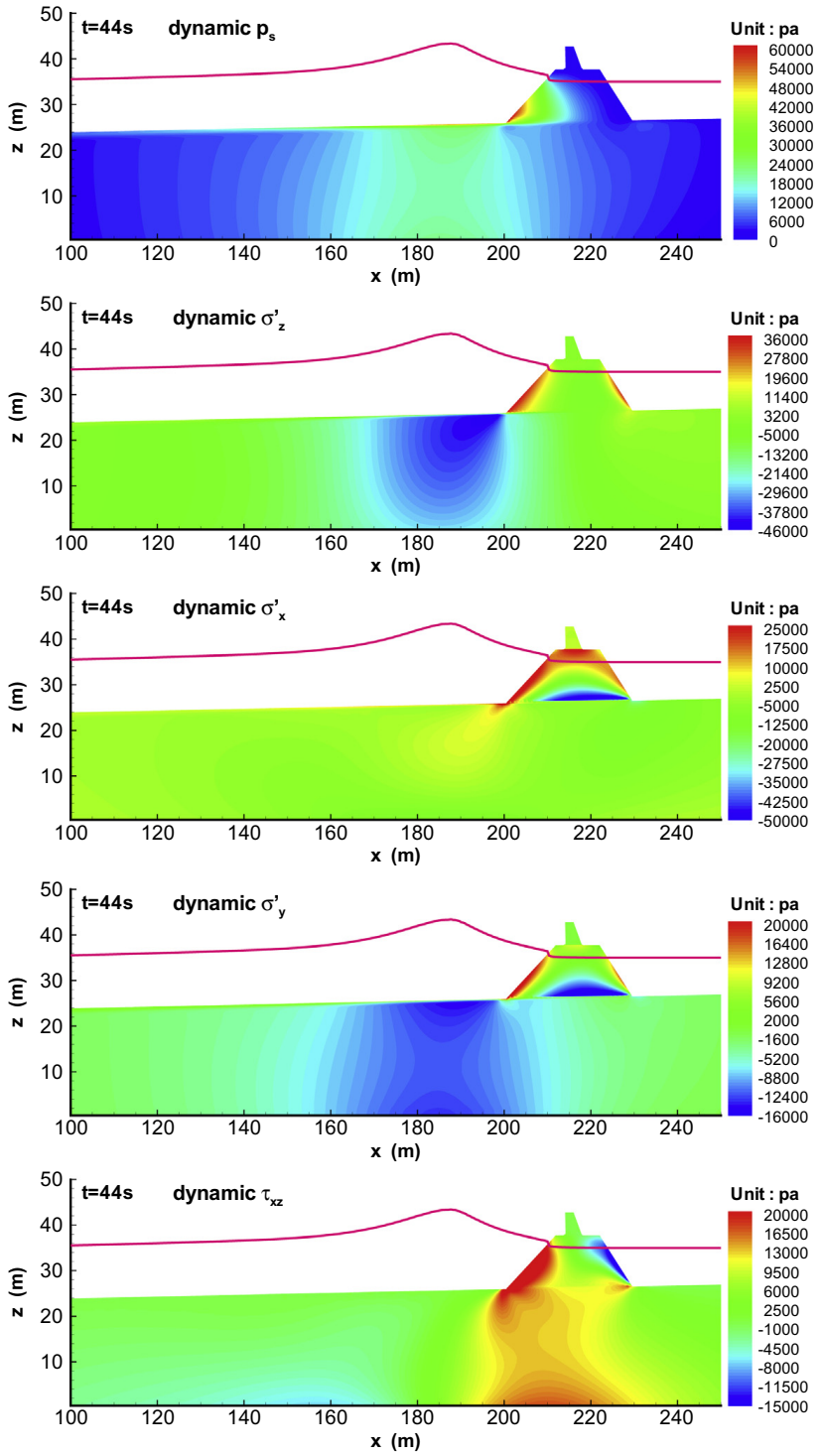

Fig. 9. Distribution of dynsmic effective stresses σ'_x, σ'_y, σ'_z and τ_{xz}, and pore pressure p_s in seabed foundation at time $t = 44$ s.

vertical effective stress σ'_z at three typical position M, N and I. M (170 m, 23.4 m) is located at the left-hand side of the breakwater; and the distance from M to the breakwater is 30 m. N (200 m, 25 m) is under the lower-left corner of the breakwater. I (230 m, 25.6) is under the lower-right corner of the breakwater. From Fig. 11, it can be found that the dynamic pore pressure and σ'_z both are zero on the three typical points before the tsunami wave arriving in the front of the breakwater. After the tsunami wave propagating to the breakwater, the pore pressure and σ'_z on the three points all increase. The maximum dynamic pore pressure on N is greater than that on the other two points. The tsunami wave induced maximum pore pressure on M is 20 kPa when there is no intensive interaction between the tsunami wave and the breakwater. When the tsunami wave is breaking, overtopping due to the block effect of the breakwater, the interaction between the tsunami wave and the breakwater is apparently intensive. The maximum pore pressure on N reaches up to 65 kPa. The dynamic pore pressure

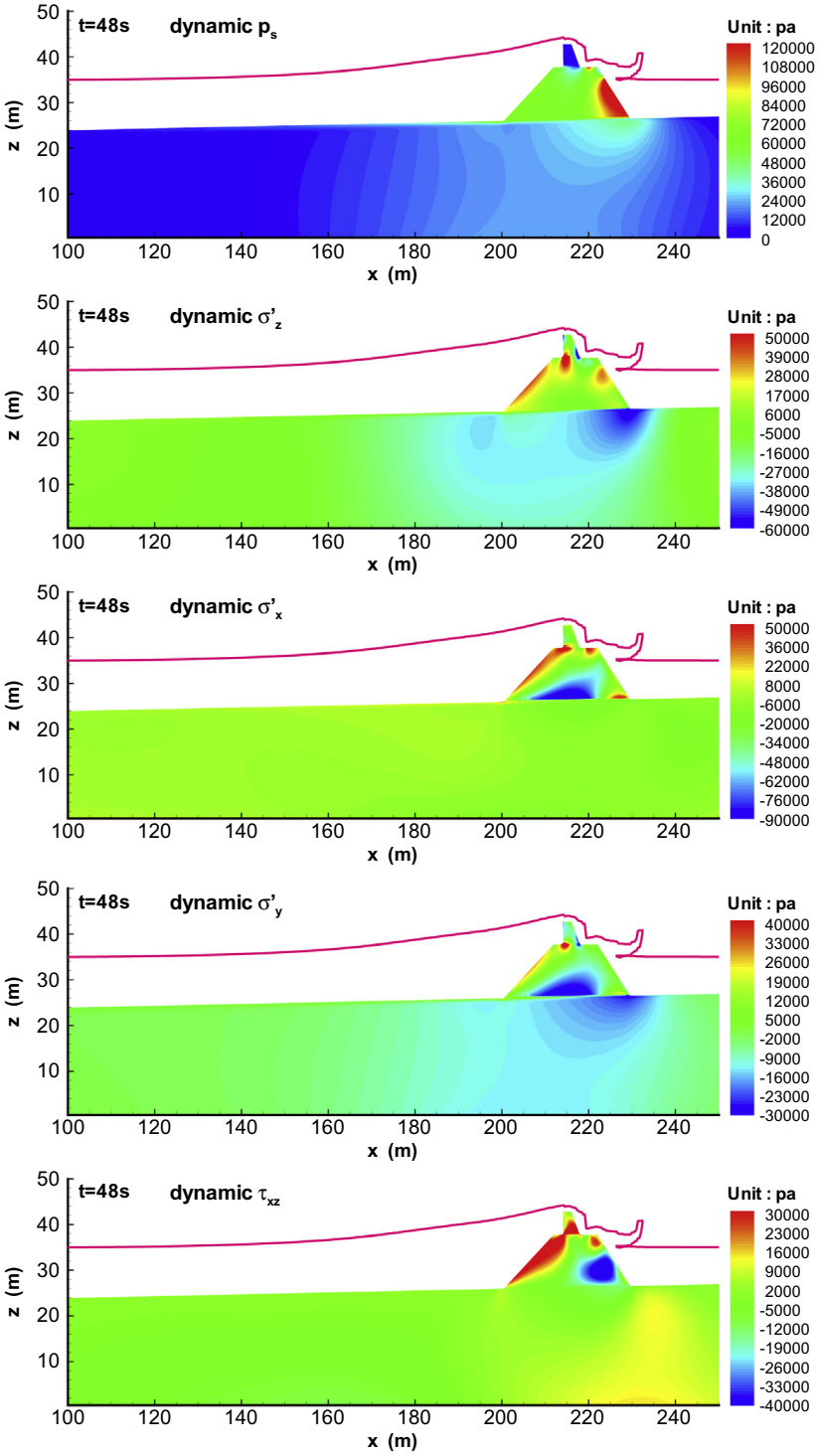

Fig. 10. Distribution of dynsmic effective stresses σ'_x, σ'_y, σ'_z and τ_{xz}, and pore pressure p_s in seabed foundation at time $t = 48$ s.

on *I* is induced by the sea water overflowing and overtopping from the left-hand side of the breakwater. The maximum dynamic pore pressure on *I* is also about 20 kPa, basically the same with that on point *M*. The maximum tsunami wave induced dynamic effective stress σ'_z on *M*, *N* and *I* are all in the range of 35 kPa to 40 kPa. The time at which the maximum dynamic response appears sequentially from left side to right side.

The seabed is a kind of porous medium, consisting of soil particles, pore water and trapped air. The soil particles form the skeleton, and the pore water and air occupies the void between the soil particles. When the tsunami wave propagating on the seabed, the seabed and breakwater is applied by a wave-induced dynamic pressure. The pore water is driven by the dynamic pressure to flow in and out the seabed. Meanwhile, the seepage force in the seabed foundation acting on the soil particles

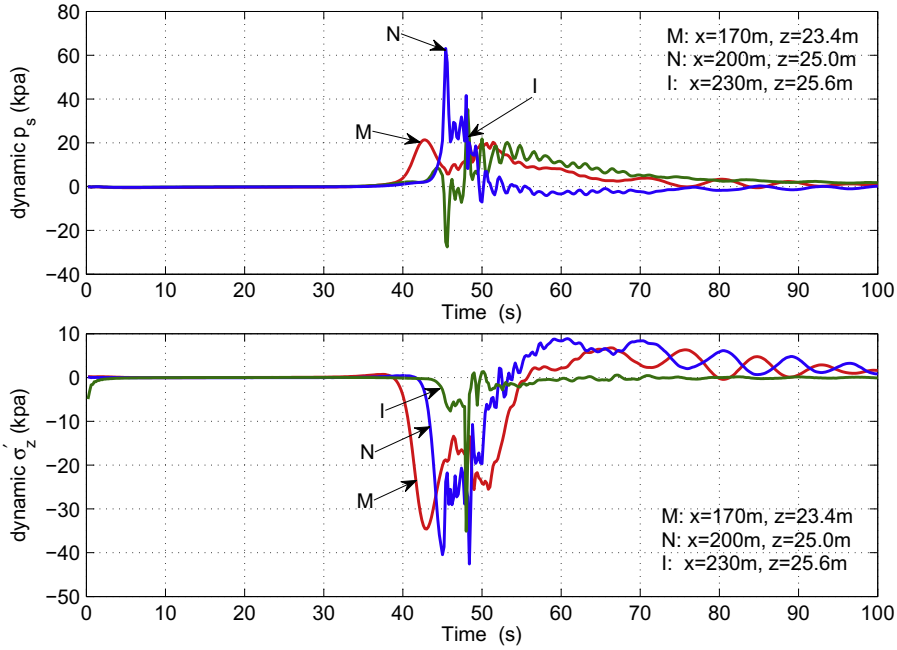

Fig. 11. Time history curve of the dynamic pore pressure p_s and vertical effective stress σ'_z at the position M, N and I.

applied by the flowing pore water is formed. The seepage force in seabed is dependent on the gradient of pore pressure in seabed, defined as:

$$j_x = \frac{\partial p_s}{\partial x} \quad \text{and} \quad j_z = \frac{\partial p_s}{\partial z}, \tag{14}$$

$$j = \sqrt{j_x^2 + j_z^2}, \tag{15}$$

where p_s is the tsunami wave induced dynamic pore pressure in the seabed foundation and breakwater.

Fig. 12 demonstrates the distribution of the seepage force in the seabed foundation and breakwater at time $t = 44$ s and $t = 48$ s. It is observed from Fig. 12 that the seepage force only appears in the zone near to the surface of the seabed foundation (the thickness is about 1 m). In the other part of the seabed foundation, the seepage force is basically near to zero. The maximum seepage force at the two typical times could reach up to 50 kN/m^3. At time $t = 44$ s, the seepage force mainly concentrates in the interface zone between the left-bottom part of breakwater and the seabed foundation. At time $t = 48$ s,

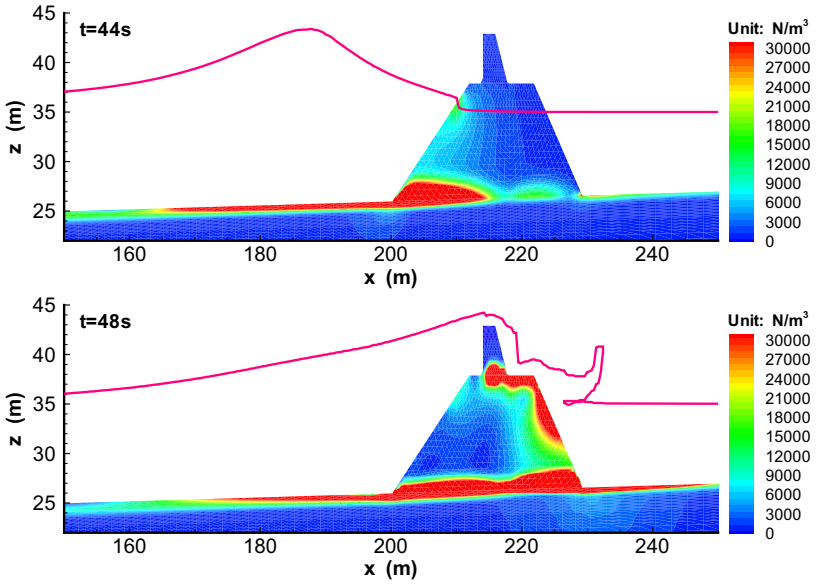

Fig. 12. The distribution of seepage force in seabed foundation and breakwater at time $t = 44$ s and $t = 48$ s.

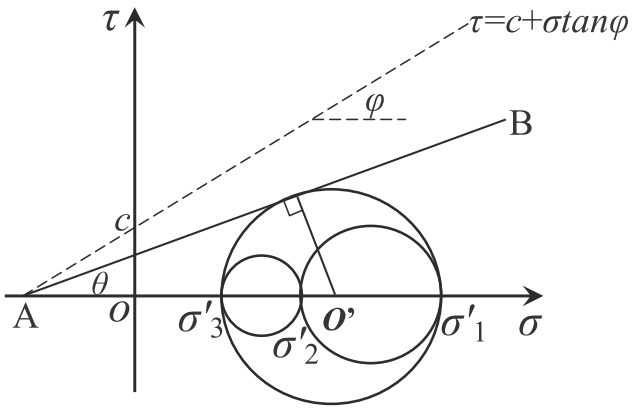

Fig. 13. Mohr-Coubomb criterion for shear failure judgement.

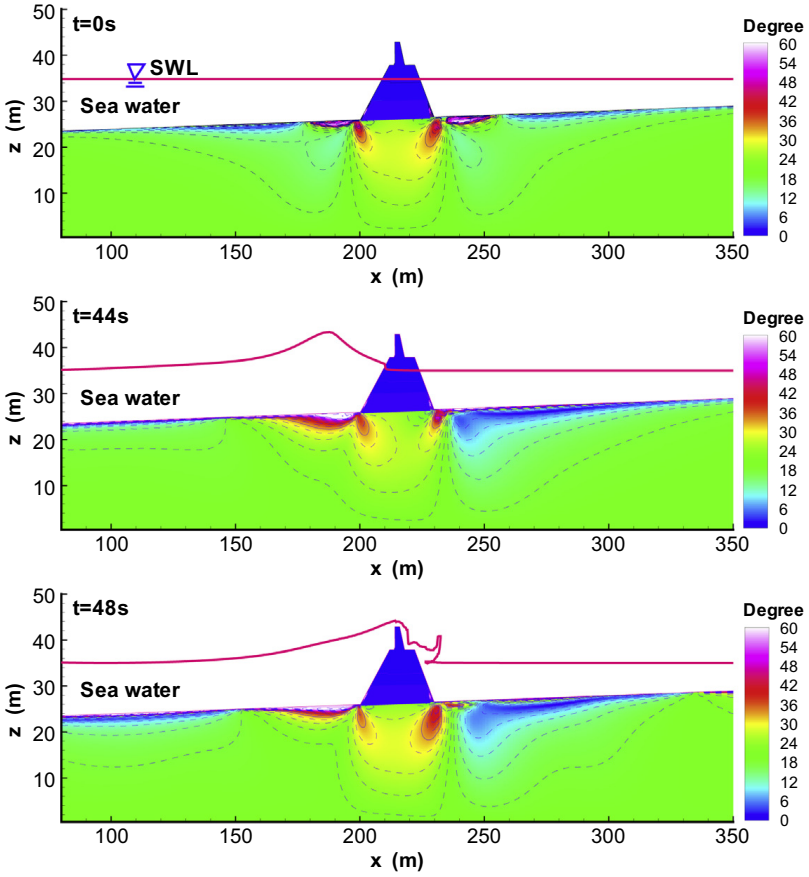

Fig. 14. Distribution of stress angle θ in the seabed foundation in the consolidation status and at time $t = 44$ s and $t = 48$ s.

the seepage force mainly concentrates in the interface zone between the whole bottom of breakwater and the seabed foundation. It is well known that the momentary liquefaction of seabed foundation is directly related to the seepage force developed in seabed. Under the wave crest, the seepage force is downward; the seabed foundation is impossible to liquefaction. Under the wave trough, the seepage force is upward, the seabed foundation would be liquefied if the upward seepage force can overcome the weight of overburdened soil and marine structures. Due to that the tsunami wave has no obvious wave trough when propagating, breaking and overtopping, the seabed foundation is unlikely to liquefy under tsunami wave loading.

4.5. Prediction of shear failure in seabed foundation

As analyzed in above section, it is impossible for the seabed foundation to liquefy under the tsunami wave loading. However, the shear failure of seabed foundation under the tsunami wave loading is quite likely to occur in the practice of engineering. In this section, we pay our attention on the shear failure of the seabed foundation under tsunami wave loading.

The Mohr–Coulomb criterion is widely used to judge the occurrence of shear failure in seabed foundation in offshore engineering. In Fig. 13, if the angle θ (known as stress angle) of the tangent AB of the maximum Mohr circle is greater or equal to the friction angle ϕ of sandy seabed foundation, the shear failure occurs at this point:

$$\theta = \arcsin\left\{\frac{\frac{\sigma'_1-\sigma'_3}{2}}{\frac{c}{\tan\phi}+\frac{\sigma'_1+\sigma'_3}{2}}\right\} \geqslant \phi, \tag{16}$$

where c and ϕ are the cohesion and friction angle of sand soil; σ'_1 and σ'_3 are the maximum and minimum principal effective stresses.

In this study, the $c = 0$, $\phi = 35^\circ$ are used for the seabed soil in computation. The distribution of stress angle θ at $t = 0$ s, 44 s and 48 s determined according to Eq. (16) are illustrated in Fig. 14. In consolidation state ($t = 0$ s), due to the construction of the breakwater on the seabed, the shear stress concentrates in the zone under the breakwater as shown in Fig. 4. The stress angle θ in the zone under the breakwater, especially under the lateral feet of the breakwater is relatively greater than that in other zone. The shear failure may occur at some points under the lateral feet of the breakwater. When the tsunami wave propagating to the breakwater at time $t = 44$ s, the effect of the tsunami wave on the distribution of stress angle θ in the seabed foundation is very significant. In the zone near to the seabed surface, and under the crest of the tsunami wave ($x = 160$ m to 200 m), the stress angle θ increases greatly under the tsunami wave loading. The shear failure will occur in this zone. Due to the fact that this zone is closed to the breakwater, the breakwater would lost its stability. When the tsunami wave is breaking, overtopping at time $t = 48$ s, the shear failure zone ($x = 160$ m to 200 m) is slightly reduced. The stress angle θ under the right foot of the breakwater increases significantly. However, the stress angle basically keeps the same in the zone near to the seabed surface, and located at the right hand side of the breakwater. The shear failure could not occur in this zone. Summarily, the tsunami wave-induced shear failure in the seabed foundation is most likely to occur in the zone located at the left hand side of breakwater, and near to the seabed surface when the tsunami wave arriving at the breakwater. Once the shear failure happening in this zone, the stability of breakwater can not be guaranteed. In the design of a marine structures in engineering, the shear failure of seabed foundation under wave loading, especially the tsunami wave loading, should be considered sufficiently.

5. Conclusion

In this study, taking the integrated model PORO-WSSI 2D as the analysis tool, in which the dynamic Biot's equation governs the soil model, and the Navier–Stokes equation governs the wave model, the dynamics of rubble mound breakwater and its seabed foundation under tsunami wave loading is investigated. In PORO-WSSI 2D, the generation and propagation of the tsunami wave is implemented by the wave model; the dynamic response of the breakwater and seabed foundation is determined by the soil model taking the pressure acting on seabed and breakwater as the boundary condition. Through analyzing, following understanding are obtained:

(1) The construction of a breakwater on seabed has significant effect on the initial consolidation state of seabed foundation. In numerical analysis, this consolidation state should be first determined, then is taken as the initial condition for the followed dynamic analysis.
(2) When the tsunami wave arriving at and passing through the breakwater, there is intensive interaction between the tsunami wave, breakwater and seabed foundation. Due to the block effect of breakwater, the tsunami wave breaks, overtops over the breakwaters. Part of wave energy is reflected by the breakwater. In this process, the tsunami wave applies a huge impact force on the lateral side of breakwater. Under this impact force loading, the breakwater moves downward and toward right side. The wave induced dynamic shear stress obviously concentrates in the zone under the breakwater. The breakwater would lose its stability in this process.
(3) The sea water overtopping and overflowing from the left hand side of breakwater makes the free surface of the sea water at the right-hand side of breakwater vibrates freely; and this vibration will finally propagate to the coastal line. The free surface of sea water at the left hand side of breakwater also vibrates freely due to the reflected wave. These two vibration of free surface of the sea water directly results in the vibration of breakwater and seabed foundation after the tsunami wave disappearing.
(4) Under the tsunami wave, the pore pressure and the vertical effective stress σ'_z in breakwater and seabed foundation increase obviously. The tsunami wave-induced seepage force mainly appears in the surface zone of seabed, and in the bottom zone of breakwater; and the seepage force are all downward. The seabed foundation is unlikely to liquefy. However, the shear failure is most likely to occur in the surface zone of seabed foundation located at the left-hand side of breakwater. This should be paid particular attentions in design of marine structures.

A real tsunami generally has a depressive leading edge when arriving at shorelines, more likely a *N*-wave. However, due to the fact that the *N*-wave is not available in the integrated model PORO-WSSI 2D at present, we adopt solitary wave to approximately simulate a tsunami wave in this work. The appropriateness of our conclusion is specially for solitary wave. For *N*-wave, the conclusion may be not applicable. More research work is needed for the problem of *N*-wave interacting with marine structures in the future.

Acknowledgments

The authors Prof. Wang and Prof. Zhu thank the financial support from Chinese 973 Project: Evolutionary Trends and Sustainable Utilization of Coral Reefs in the South China Sea (2013CB956104). The author Dr. Ye Jianhong and Professor Jeng D-S are grateful for the financial support from EPSRC#EP/G006482/1. The author Ye Jianhong also appreciates the funding support of Overseas Research Student Award from Scottish Government, UK.

References

[1] J.H. Ye, Numerical analysis of wave-seabed-breakwater interactions, Ph.D. Thesis, Universtity of Dundee, Dundee, UK, 2012.
[2] M. Tanaka, J.W. Dold, M. Lewy, D.H. Peregrine, Instability and breaking of a solitary wave, J. Fluid Mech. 185 (1987) 235–248.
[3] Y. Li, F. Raichlen, Non-breaking and breaking solitary wave run-up, J. Fluid Mech. 456 (2002) 295–318.
[4] S.-C. Hsiao, T.-W. Hsu, T.-C. Lin, Y.-H. Chang, On the evolution and run-up of breaking solitary waves on a mild sloping beach, Coastal Eng. 55 (12) (2008) 975–988 (Cited by (since 1996) 9).
[5] S.T. Grilli, M.A. Losada, F. Martin, Characteristics of solitary wave breaking induced by breakwaters, J. Waterway Port Coastal Ocean Eng. ASCE 120 (1) (1994) 74–92.
[6] K. Fujima, Effect of a submerged bay-mouth breakwater on tsunami behavior analyzed by 2d/3d hybrid model simulation, Water Pollut. 39 (2) (2006) 179–193 (Handbook of Environmental Chemistry, Volume 5).
[7] C.J. Huang, H.H. Chang, H.H. Hwung, Structural permeability effects on the interaction of a solitary wave and a submerged breakwater, Coastal Eng. 49 (1–2) (2003) 1–24.
[8] S.-C. Hsiao, T.-C. Lin, Tsunami-like solitary waves impinging and overtopping an impermeable seawall: experimental and RANS modeling, Coastal Eng. 57 (1) (2010) 1–18.
[9] H. Xiao, Y.L. Young, J.H. Prevost, Hydro- and morpho-dynamic modeling of breaking solitary waves over a fine sand beach. Part II: Numerical simulation, Mar. Geolo. 269 (3–4) (2010) 119–131.
[10] Y.L. Young, J.A. White, H. Xiao, R.I. Borja, Liquefaction potential of coastal slopes induced by solitary waves, Acta Geotech. 4 (1) (2009) 17–34.
[11] H. Xiao, Y.L. Young, J.H. Prevost, Parametric study of breaking solitary wave induced liquefaction of coastal sandy slopes, Ocean Eng. 37 (17–18) (2010) 1546–1553.
[12] N. Mizutani, A. Mostarfa, K. Iwata, Nonliear regular wave submerged breakwater and seabed dynamic interaction, Coastal Eng. 33 (1998) 177–202.
[13] A. Mostafa, N. Mizutani, K. Iwata, Nonlinear wave composite breakwater and seabed dynamic interaction, J. Waterway Port Coastal Ocean Eng. 25 (2) (1999) 88–97.
[14] M.A. Biot, General theory of three dimensional consolidation, J. Appl. Phys. 12 (2) (1941) 155–164.
[15] M.A. Biot, The theory of propagation of elastic waves in a fluid-saturated porous solid. Low-frequency range, J. Acoust. Soc. Am. 28 (2) (1956) 168–178.
[16] J.H. Ye, D.-S. Jeng, R. Wang, C. Zhu, Validation of a 2-D semi-coupled numerical model for fluid–structure–seabed interaction, J. Fluids Struct. (2013), http://dx.doi.org/10.1016/j.jfluidstructs.2013.04.008.
[17] O.C. Zienkiewicz, C.T. Chang, P. Bettess, Drained undrained consolidating and dynamic behaviour assumptions in soils, Geotechnique 30 (4) (1980) 385–395.
[18] O.C. Zienkiewicz, A.H.C. Chan, M. Pastor, B.A. Schrefler, T. Shiomi, Computational Geomechanics with Special Reference to Earthquake Engineering, John Wiley and Sons, England, 1999.
[19] T.J. Hsu, T. Sakakiyama, P.L.F. Liu, A numerical model for wave motions and turbulence flows in front of a composite breakwater, Coastal Eng. 46 (2002) 25–C50.
[20] P.L.F. Liu, P.Z. Lin, K.A. Chang, T. Sakakiyama, Numerical modeling of wave interaction with porous structures, J. Waterway Port Coastal Ocean Eng. ASCE 125 (1999) 322–330.
[21] P. Lin, S.A.S.A. Karunarathna, Numerical study of solitary wave interaction with porous breakwaters, ASCE J. Waterway Port Coastal Ocean Eng. 133 (5) (2007) 352–363.
[22] P. Lin, P.L.F. Liu, A numerical study of breaking waves in the surf zone, J. Fluid Mech. 359 (1998) 239–264.
[23] Z.P. Lin, P.L.-F. Liu, Internal wave-maker for Navier–Stokes equations models, J. Waterway Port Coastal Ocean Eng. 99 (4) (1999) 207–215.
[24] J.R. Hsu, D.S. Jeng, Wave-induced soil response in an unsaturated anisotropic seabed of finite thickness, Int. J. Numer. Anal. Methods Geomech. 18 (11) (1994) 785–807.
[25] H.B. Lu, The Research on Pore Water Pressure Response to Waves in Sandy Seabed, Ph.D. Thesis, Changsha University of Science and Technology, Changsha Hunan China, 2005.
[26] C.P. Tsai, T.L. Lee, Standing wave induced pore pressure in a porous seabed, Ocean Eng. 22 (6) (1995) 505–517.
[27] D.-S. Jeng, J.H. Ye, J.-S. Zhang, P.-F. Liu, An integrated model for the wave-induced seabed response around marine structures: model verifications and applications, Coastal Eng. 72 (1) (2013) 1–19.
[28] T. Nakayama, Boundary element analysis of nonlinear water wave problem, Int. J. Numer. Method Eng. 19 (1983) 953–970.